



## Graphene nanoscrolls encapsulated $\text{TiO}_2$ (B) nanowires for lithium storage



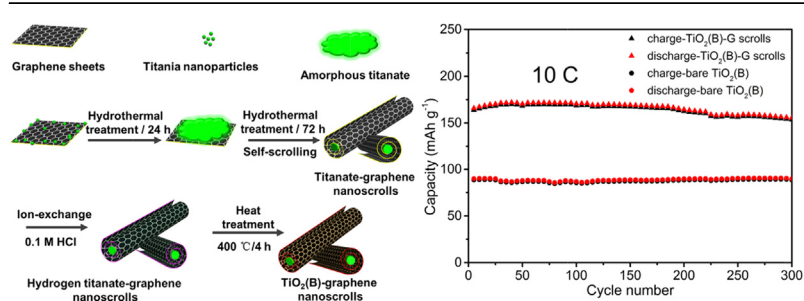
Xinlu Li\*, Yonglai Zhang, Tongtao Li, Qineng Zhong, Hongyi Li, Jiamu Huang

College of Materials Science and Engineering, Chongqing University, Chongqing 400030, PR China

### HIGHLIGHTS

- Graphene nanoscrolls encapsulated  $\text{TiO}_2$  (B) nanowires are constructed for the first time.
- Graphene nanoscrolls effectively stabilize the structure of the architectures.
- The reversible capacity remains  $153 \text{ mAh g}^{-1}$  at  $10 \text{ C}$  after 300 cycles.

### GRAPHICAL ABSTRACT



### ARTICLE INFO

#### Article history:

Received 2 March 2014

Received in revised form

9 June 2014

Accepted 10 June 2014

Available online 18 June 2014

#### Keywords:

Graphene nanoscrolls

Titanium dioxide (B)

Anode materials

Lithium ion batteries

### ABSTRACT

Graphene nanoscrolls encapsulated  $\text{TiO}_2$  (B) nanowires have been fabricated through a self-scrolling and template-free process for the first time. Transmission electron microscope images reveal that graphene tightly encompassed  $\text{TiO}_2$  (B) nanowires to construct nanoscrollled architectures. Cyclic voltammetry demonstrates that pseudocapacitive behavior dominates fast lithium storage rather than diffusion-controlled insertion in the hybrids. Galvanostatic cycling tests show that the reversible specific capacity of the hybrids remains  $153 \text{ mAh g}^{-1}$  after 300 cycles at  $10 \text{ C}$  with capacity retention of 94%. The excellent lithium storage performance can be attributed to the unique nanoscrollled structure, which provides abundant channels for lithium ions transport, as well as accommodates volume variation during fast lithiation and delithiation.

© 2014 Elsevier B.V. All rights reserved.

### 1. Introduction

The rapid development of portable digital devices, plug-in hybrid and electric vehicles provokes the urgent demand for rechargeable batteries [1]. High-performance lithium ion batteries offer a promising solution to meet the requirement of high energy storage and power density. To date, one of the most widespread anode materials in commercial lithium ion batteries is graphite, due to its low cost and feasible process. However, the formation of solid-electrolyte interphase (SEI) on the graphite surface during the

initial cycle consumes lots of solvated lithium ions, leading to irreversible capacity loss [2]. Furthermore, the poor cycling performance of graphite at high current density restricts its large-scale application in high-power density batteries. Recently, transition metal oxides, such as  $\text{SnO}_2$  [3] and  $\text{MnO}_2$  [4], have attracted extensive attention owing to their safe working potentials, high specific capacities and cost-effectiveness. Among them, titanium dioxide ( $\text{TiO}_2$ ) with multi-polymorphs (anatase, rutile, and  $\text{TiO}_2$  (B)) has been widely investigated in terms of their natural abundance and environmental benignity [5,6].  $\text{TiO}_2$  (B) is considered to be a desirable alternative anode material for high-power density batteries because of its high operating potential ( $\sim 1.7 \text{ V}$ ) and structural stability during lithiation and delithiation [7,8]. Particularly, it has been demonstrated that the lithium insertion in  $\text{TiO}_2$  (B) via

\* Corresponding author. Tel.: +86 23 65127940; fax: +86 23 65127306.

E-mail address: [lixinlu@cqu.edu.cn](mailto:lixinlu@cqu.edu.cn) (X. Li).

pseudocapacitance mechanism [9,10], rather than solid-state diffusion observed in anatase [11–13] and rutile [14]. Therefore, enormous efforts have been devoted to the synthesis of  $\text{TiO}_2$  (B) with various nanostructures, such as nanoparticles [15,16], nanowires [17], nanotubes [18,19] and nanosheets [20]. Nanostructured  $\text{TiO}_2$  (B) with large specific area can effectively shorten the distance of lithium ion diffusion [7,20], thus accelerate the transport of lithium ions. However, the poor electronic conductivity and self-aggregation of nanostructured  $\text{TiO}_2$  (B) impede the charge transfer in the electrodes [21].

Carbon nanomaterials, such as carbon nanotubes and graphene, have been widely utilized as substrates or conductive additives to overcome the issues [22–26]. Kavan et al. [27] reported that multi-walled carbon nanotubes, which were oxidative functionalized by carboxylic groups, exhibited better affinity towards  $\text{TiO}_2$  and the electrochemical performance of  $\text{TiO}_2$  was improved by carbon nanotubes networking. Tremendous endeavor has been undertaken to synthesize graphene-based  $\text{TiO}_2$  composites with good electronic conductivity for high performance rechargeable batteries. Lou et al. [28] prepared graphene-wrapped  $\text{TiO}_2$  hollow structures via simple electrostatic interaction, which exhibited improved cycle performance. Feng et al. [29] synthesized sandwich-like, graphene-based mesoporous titania nanosheets with silica templates, which performed outstanding rate capabilities. Nevertheless, transition metal oxides loading on the graphene nanosheets tend to pulverize and peel off the substrate during the process of  $\text{Li}^+$  insertion and extraction, resulting in poor cycling performance [30]. Graphene nanoscrolls, which are composed of several roll-up graphene nanosheets and open-ended with a tubular hollow structure but not seamless [31–35], are considered to be an ideal substrate to combine electrode active materials, wherein tubular cavities can provide the channels for ions transport while graphitic planes on the outside facilitate the charge transfer at high rates. However, to the best of our knowledge, there have been few reports on graphene nanoscrolls-based composites for LIBs.

In this work, we introduce a facile template-free method to construct  $\text{TiO}_2$  (B)-graphene nanoscrolls ( $\text{TiO}_2$  (B)-G scrolls). Graphene oxide and anatase  $\text{TiO}_2$  powder were mixed and hydrothermally treated, followed by ion-exchange and heat treatment to synthesize graphene nanoscrolls encapsulated  $\text{TiO}_2$  (B) nanowires. The hybrids of  $\text{TiO}_2$  (B)-graphene nanoscrolls exhibit excellent lithium storage capacity and rate capability at high current densities. This green synthesis access provides a feasible pathway to large-scale fabrication of graphene nanoscrolls-based composites for advanced lithium ion batteries.

## 2. Experimental

### 2.1. Preparation of graphene nanoscrolls encapsulated $\text{TiO}_2$ (B) nanowires

Graphite oxide (GO) was prepared from natural graphite powder with a modified Hummers method. Briefly, 3 g of graphite powder and 1.5 g of sodium nitrate were placed in a 1000 mL flask, 120 mL of concentrated sulfuric acid was slowly dropped into the flask in an ice bath, and then 9 g of potassium permanganate was added in 30 min under stirring for another 4 h. After continuously stirred for 1 h in water bath at 35 °C, the reaction temperature was increased to 95 °C and kept for 30 min. Excessive 15 mL of hydrogen peroxide (30 wt%) was dumped into the mixture to make bright yellow solution. After repeated centrifugation until neutral (pH = 7) with excessive deionized water (DI), graphite oxide was obtained.

After expansion, 70 mg of graphene oxide was dispersed in 20 mL of deionized water under ultrasonication for 1 h to make

homogeneous dispersion. After 1 g of commercial  $\text{TiO}_2$  powder (anatase, 40–100 nm) was added, the mixture was stirred for 4 h at ambient temperature. 30 mL of 10 M NaOH aqueous solution was added into the mixture, and then the mixture was transferred to 100 mL of Teflon-lined stainless autoclave at 150 °C for 72 h. The as-obtained suspension was stirred with 0.1 M HCl solution for 24 h, then washed with DI until neutral (pH = 7), dried at 80 °C, followed by annealing at 400 °C in  $\text{N}_2$  for 4 h to prepare graphene nanoscrolls encapsulated  $\text{TiO}_2$  (B) nanowires. A similar procedure was conducted without graphene oxide and annealed in air to synthesize bare  $\text{TiO}_2$  (B).

### 2.2. Materials characterization

The specific surface area and pore structure analysis were investigated by nitrogen adsorption at 77 K (Micromeritics ASAP 2020). X-ray diffraction (XRD) patterns were recorded on DMAX-2500 PC X-ray spectrometer with  $\text{Cu K}\alpha$  radiation ( $\lambda = 1.5406 \text{ \AA}$ ) at a scanning speed of 4° min<sup>-1</sup>. The morphology and crystalline microstructure of the products were characterized by field emission scanning electron microscope (FESEM, ZEISS AURIGA FIB-SEM) and high-resolution transmission electron microscope (HRTEM, LIBRA 200 FE at 200 kV). Raman spectra were examined on micro-Raman spectroscope (JY HR800) using 633 nm incident radiation. Fourier Transform infrared (FTIR) spectrometry was conducted on Thermo Nicolet (Nicolet 5DXC) with KBr incorporated pellet. Thermogravimetry (TG) analysis was performed in the temperature range of 25–800 °C in air with a Netzsch STA 449C thermal analyzer.

### 2.3. Electrochemical measurements

Electrochemical tests were carried out using CR2430 coin-type cells assembled and compacted under 8 MPa gas-pressure in a glove box filled with dry argon atmosphere. Lithium foil was both used as the counter electrode and reference electrode. The working electrodes were fabricated by the slurry composed of the active material, carbon black, and poly (vinylidene fluoride) (PVDF) in a weight ratio of 70:15:15 in N-methyl-2-pyrrolidone (NMP). To avoid the influence of the electrochemical response of working electrode, the diameter of counter electrode (20 mm) is larger than that of working electrode (16 mm). The electrolyte used was 1 M  $\text{LiPF}_6$  in a mixture of ethylene carbonate (EC) and diethyl carbonate (DEC) (1:1, v/v), and microporous polypropylene film (Celgard 2500) was used as the separator. Cyclic voltammetry (CV) tests were measured on an electrochemical workstation (Solartron 1287 + 1260 8w) between 1.0 and 3.0 V at various scan rates of 0.1–1 mV s<sup>-1</sup>. Galvanostatic charge–discharge cycling tests were conducted using a battery test system (Arbin BT 2000) in a voltage window of 1.0–3.0 V at different current densities.

## 3. Results and discussion

Graphene oxide is highly amphiphilic with epoxy and hydroxyl groups on the basal plane while carboxyls, anhydrides, phenols on the edge [36]. When dispersed in water under ultrasonication, titania nanoparticles are likely to anchor on the oxidized graphene nanosheets to form homogeneous suspension. As illustrated in Fig. 1, when the suspension of graphene oxide and  $\text{TiO}_2$  nanoparticles are hydrothermally treated in alkali solution, amorphous titanate intermediates generate and attach on the oxidized graphene nanosheets, successively contract and transform to titanate nanowires after hydrothermal treatment. At the same time, graphene nanosheets are scrolled up to encapsulate titanate nanowires inside under the strong adhesion between graphene

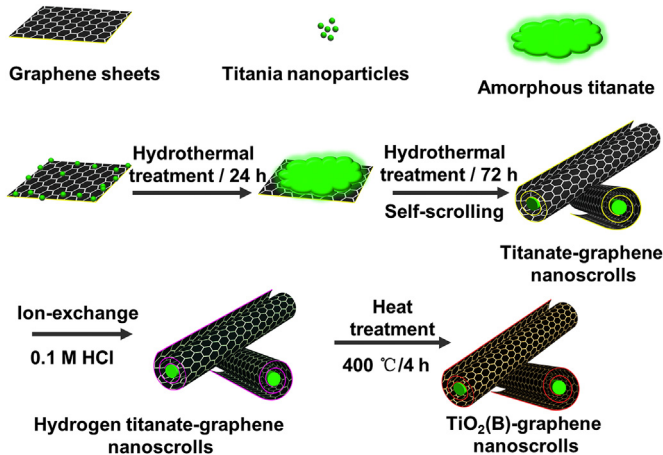


Fig. 1. Schematic illustration of  $\text{TiO}_2$  (B)-graphene nanoscrolls synthesis process.

nanosheets and the intermediates, resulting in nanoscrollled architectures. After ion-exchange and annealing, the hybrids of graphene nanoscrolls encapsulated  $\text{TiO}_2$  (B) nanowires are synthesized. Additionally, bare  $\text{TiO}_2$  (B) nanowires form under the same synthesis condition without graphene addition (as shown in Fig. S3).

The morphology and microstructure of the as-prepared products were analyzed by transmission electron microscopy (TEM). As shown in Fig. 2,  $\text{TiO}_2$  (B)-graphene nanoscrolls lie randomly and stretch straightly with diameters of *ca.* 200 nm. Obviously, both the front view of rolls in Fig. 2(b) and back view of rolls in Fig. 2(e) clearly confirm the nanoscrollled structure of the composites. Fig. 2(a) and (d) show the corresponding structural illustrations. Notably, the thickness of graphene nanoscrolls is about 12 nm in Fig. 2(b) while 32 nm in Fig. 2(e), the thickness of graphene nanoscrolls beyond  $\text{TiO}_2$  (B) nanowires is dependent on the initial graphene layers and the driving force of rolling up from titanate intermediates. The selected-area electron diffraction (SAED) patterns (insets of Fig. 2(b) and (e)) confirm the structure of

monoclinic  $\text{TiO}_2$  (B). The lattice fringes with a *d*-spacing of 3.57 Å in Fig. 2(c) and 3.52 Å in Fig. 2(f), corresponding to the (110) lattice plane of  $\text{TiO}_2$  (B). The corresponding  $d_{110}$  values in our samples vary slightly with different observing spots. It should be noted that graphene nanoscrolls possibly have an influence in the change of  $d_{110}$  spacing during the formation  $\text{TiO}_2$  (B) nanocrystals. The (110) plane is found perpendicular to the nanowires, suggesting that the nanowires grow along the *ab* plane of  $\text{TiO}_2$  (B). [20] It can also be seen from the HRTEM images that  $\text{TiO}_2$  (B) nanowires own larger lattice fringes, which are presumably associated with the mutual influence between the titanates and graphene nanosheets during scrolling process, comparing with the data from JCPDS 74-1940. The enlarged *d*-spacing between crystal facets is beneficial to ions diffusion, which favors fast insertion and extraction of lithium ions during pseudocapacitive reaction [16]. It is worth noting that graphene nanoscrolls are porous (Fig. 2(c) and (f)) owing to alkali “etching” [37] and greatly deoxygenated [38], which effectively facilitate the ions transfer and diffusion.

Nitrogen isothermal adsorption–desorption measurements were performed to investigate the Brunauer–Emmett–Teller (BET) specific surface area and the porosity of bare  $\text{TiO}_2$  (B) and  $\text{TiO}_2$  (B)-graphene nanoscrolls. Fig. 3(a) shows the isotherm curves of the as-prepared  $\text{TiO}_2$  (B)-graphene nanoscrolls, which is a typical Type IV isotherm [39] with a clear hysteresis loop at the relative pressure of 0.6–1.0, indicating porosity in the composites. The specific surface area of  $\text{TiO}_2$  (B)-graphene nanoscrolls is  $51.1 \text{ m}^2 \text{ g}^{-1}$ , slightly larger than that of the bare  $\text{TiO}_2$  (B) ( $47.2 \text{ m}^2 \text{ g}^{-1}$ ). The pore size distribution is between 1 and 4 nm, which facilitates  $\text{Li}^+$  transport. The as-made products were characterized by powder X-ray diffraction analysis. As shown in Fig. 3(b), the peaks appear to be broadened and shift to smaller diffraction angles, indicating larger *d*-spacing between crystalline facets (coincides with HRTEM patterns in Fig. 2(d) and (f)). The main peaks can be indexed to the monoclinic  $\text{TiO}_2$  (B) phase (JCPDS 74-1940), whereas weak diffraction of anatase phase can be detected. The small amount of anatase in the final products may originate from the residual raw anatase  $\text{TiO}_2$  nanoparticles or the partial phase transformation of  $\text{TiO}_2$  (B) during heat treatment (XRD pattern of hydrated titanate in Fig. S4), which is unavoidable according to previous report [19]. However, no

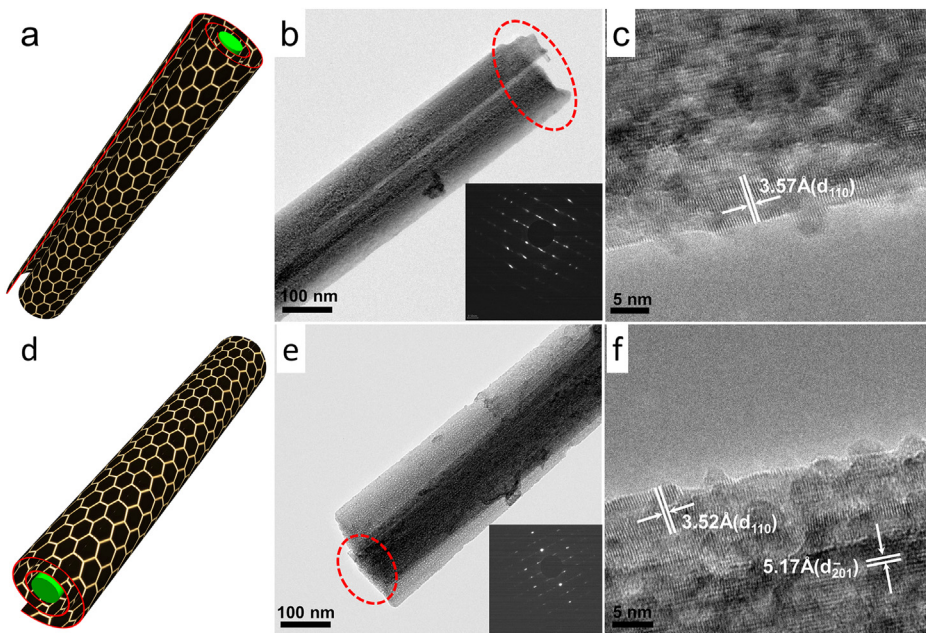
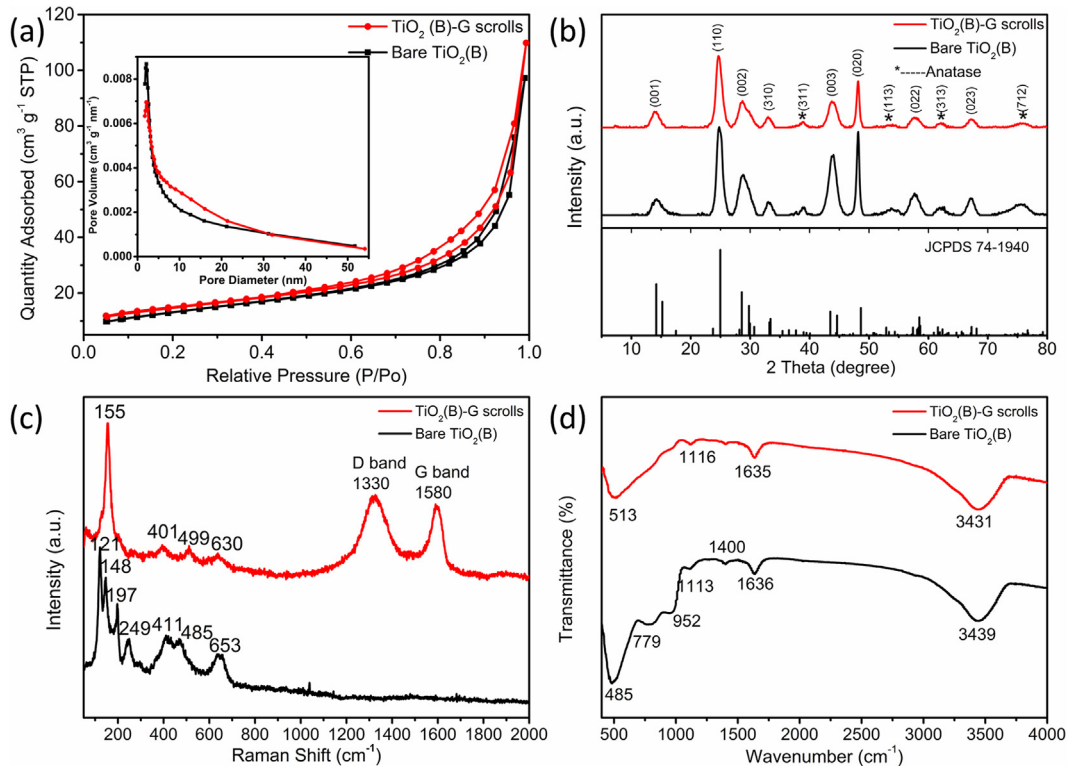


Fig. 2. Front view of (a) a structural illustration, (b) typical  $\text{TiO}_2$  (B)-graphene nanoscrolls and (c) corresponding HRTEM image; back view of (d) a structural illustration, (e) typical  $\text{TiO}_2$  (B)-graphene nanoscrolls and (f) corresponding HRTEM image. Insets of (b) and (e) show the corresponding SAED patterns, respectively.



**Fig. 3.** (a) N<sub>2</sub> adsorption-desorption isothermal curves and pore size distribution (inset), (b) X-ray diffraction patterns, (c) Raman spectra, (d) FTIR spectra of bare TiO<sub>2</sub> (B) and TiO<sub>2</sub> (B)-graphene nanoscrolls.

obvious diffraction peaks of graphene in the composites could be detected due to its low weight ratio (~5.4 wt%, see Fig. S5) and weak diffraction intensity. The diffraction of (002) plane is probably overlapped by the diffraction of (110) plane of TiO<sub>2</sub> (B).

Raman spectroscopy is quite well-suited to characterize TiO<sub>2</sub> polymorphs due to their distinct vibrational modes, as well as noncrystalline phases. As shown in Fig. 3(c), the bands below 200 cm<sup>-1</sup> are associated with the low-energy Ti–O–Ti torsional and bending modes, while the broadened bands between 400 and 500 cm<sup>-1</sup> may be ascribed to amorphous TiO<sub>2</sub> intermediates or hydrogen titanate impurities [16]. The high-wavenumber region (500–1000 cm<sup>-1</sup>) obviously shows the existence of bands shift toward the high-frequency region, which are mostly connected to Ti–O–Ti stretching vibrations [21]. The D band (1330 cm<sup>-1</sup>) and G band (1580 cm<sup>-1</sup>) in the spectrum of TiO<sub>2</sub> (B)-graphene nanoscrolls prove the existence of graphitic (sp<sup>2</sup>) carbon [40]. Notably, the shift of 155 cm<sup>-1</sup> in TiO<sub>2</sub> (B)-graphene nanoscrolls is quite sharp, which is due to the surface strain induced during self-scrolling process [21]. The FTIR spectra of bare TiO<sub>2</sub> (B) and TiO<sub>2</sub> (B)-graphene nanoscrolls are shown in Fig. 3(d). The broad absorption peak at ~3430 cm<sup>-1</sup> is related to the stretching vibrations of hydroxyls, and the band at ~1630 cm<sup>-1</sup> is connected to the O–H bending modes of water molecules. The absorption peak at about 1110 cm<sup>-1</sup> corresponds to the asymmetric stretching vibration of Ti–O bond [25], corroborating the structure of titania. While the broad absorption bands ranged from 500 to 1000 cm<sup>-1</sup> are associated with the stretching vibration of Ti–O–Ti bond. However, no obvious adsorption peaks appear between 600 and 1000 cm<sup>-1</sup> in the spectrum of TiO<sub>2</sub> (B)-graphene nanoscrolls, owing to the restraint from the tightly encapsulated graphene nanoscrolls beyond TiO<sub>2</sub> (B) nanowires [21].

Cyclic voltammetry (CV) was used to investigate the electrochemical behaviors of bare TiO<sub>2</sub> (B) nanowires and TiO<sub>2</sub> (B)-graphene nanoscrolls. Fig. 4(a) shows the cyclic voltammograms of the

bare TiO<sub>2</sub> (B) electrode at a slow scan rate of 0.02 mV s<sup>-1</sup>. Two pairs of cathodic/anodic S-peaks displayed in the first cycle at ca. 1.5/1.6 V and 1.6/1.7 V are denoted as S1 and S2, respectively, which are associated with pseudocapacitive lithium storage behavior of TiO<sub>2</sub> (B) [7,9]. A pair of peaks at 1.7/2.0 V (denoted as A peak) are assigned to the solid-state diffusion of lithium insertion in the anatase TiO<sub>2</sub> [20,39]. In the following two cycles, the peak potentials and curve shapes almost overlap, showing good cycling stability of lithiation and delithiation in bare TiO<sub>2</sub> (B). The CV measurements at various scan rates of 0.1–1.0 mV s<sup>-1</sup> (Fig. 4(b)) imply that the peak currents of S-peaks increase much faster than those of A-peaks, demonstrating that pseudocapacitive Li<sup>+</sup> insertion plays a dominant role in TiO<sub>2</sub> (B) at high current densities, as the A-peaks disappear with the scan rates increase [41]. Notably, the areas of CV curves of TiO<sub>2</sub> (B)-graphene nanoscrolls are obviously larger than bare TiO<sub>2</sub> (B), indicating higher specific capacity, and the CV shapes of TiO<sub>2</sub> (B)-graphene nanoscrolls are much broader than bare TiO<sub>2</sub> (B), similar to a typical pseudocapacitive behavior. Both the cyclic voltammograms of the TiO<sub>2</sub> (B)-graphene nanoscrolls electrode in Fig. 4(c) (at a scan rate of 0.02 mV s<sup>-1</sup>) and Fig. 4(d) (at various scan rates) verify that pseudocapacitive behavior governs in TiO<sub>2</sub> (B) nanowires.

The capacitive response is mainly associated with the pseudocapacitive effects (Equation (1)) and diffusion-controlled insertion processes (Equation (2)), where  $k_1 v$  and  $k_2 v^{1/2}$  correspond to the current contributions from the surface capacitive effects and the diffusion-controlled insertion process, respectively [11].

$$i(V) = k_1 v \quad (1)$$

$$i(V) = k_2 v^{1/2} \quad (2)$$

Insets of Fig. 4(b) and (d) display the plots of S-peak currents vs. scan rates of bare TiO<sub>2</sub> (B) and TiO<sub>2</sub> (B)-graphene nanoscrolls,

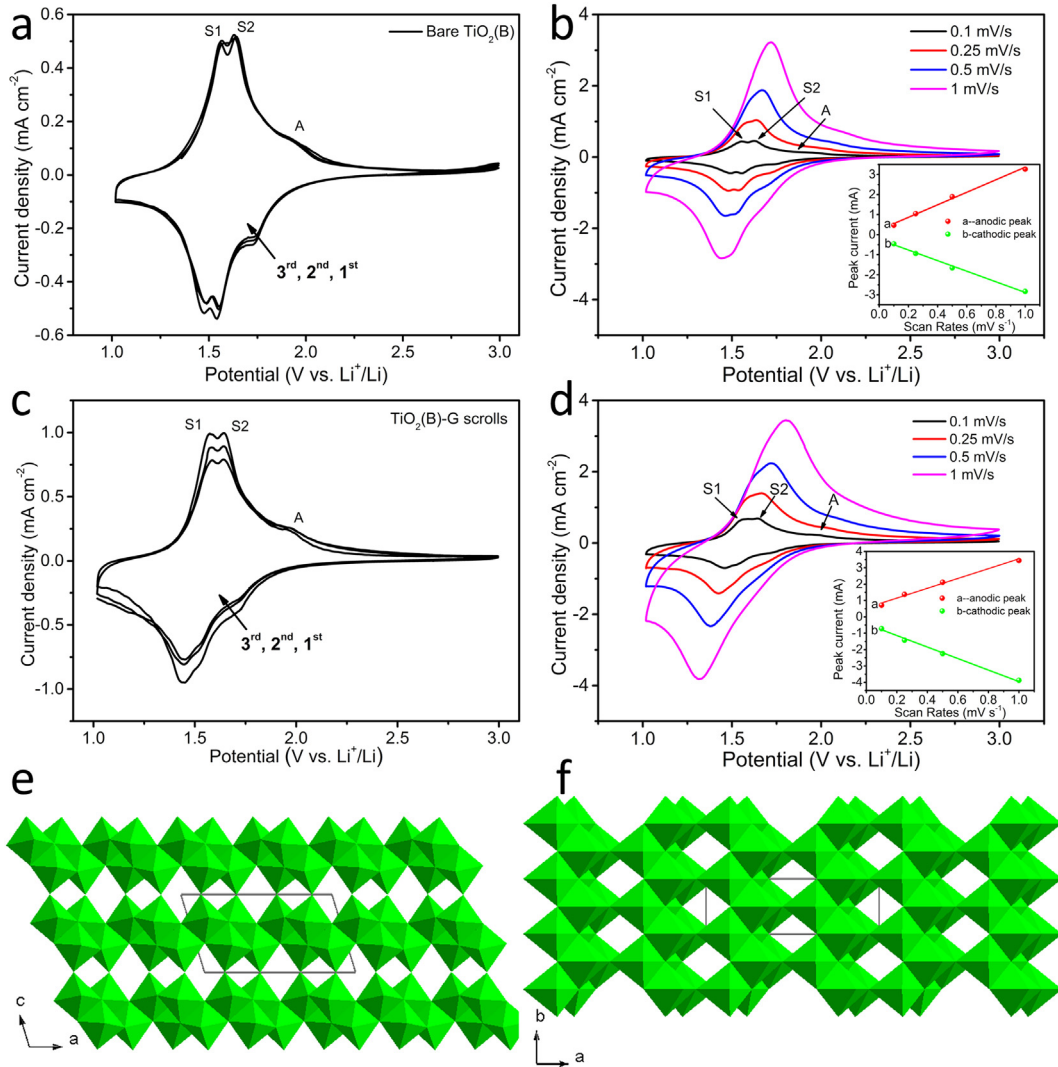


**Fig. 4.** Cyclic voltammograms of bare  $\text{TiO}_2$  (B) and  $\text{TiO}_2$  (B)-graphene nanoscrolls: (a), (c) at a scan rate of  $0.02 \text{ mV s}^{-1}$ ; (b), (d) at different scan rates between  $0.1$  and  $1.0 \text{ mV s}^{-1}$  in the potential window of  $1.0$ – $3.0$  V, insets show the S-peak currents vs. scan rates, respectively. Crystal models of  $\text{TiO}_2$  (B) with the direction parallel to (e)  $b$ -axis and (f)  $c$ -axis, respectively.

respectively, where the currents are linear with scan rates, further confirming the dominant pseudocapacitive effects. Notably, the peak currents of  $\text{TiO}_2$  (B)-graphene nanoscrolls are much higher than those of the bare  $\text{TiO}_2$  (B) owing to the graphene nanoscrolls outside which significantly enhance the electronic conductivity of the hybrids.  $\text{TiO}_2$  (B) adopts a monoclinic structure, which is composed of edge- and corner-sharing  $\text{TiO}_6$  octahedra with an open channel parallel to the  $b$ -axis that sits between axial oxygens (crystal models of  $\text{TiO}_2$  (B) are shown in Fig. 4(e) and (f)) [10,42]. Previous studies have verified that the channels parallel to the  $b$ -axis and  $c$ -axis in  $\text{TiO}_2$  (B) lattice favored  $\text{Li}^+$  transport, thus unveiling that  $\text{Li}^+$  insertion/extraction rates could be greatly increased by reducing the path parallel to  $b$ - and  $c$ -axis [41,43].

The discharge/charge cycling performances of bare  $\text{TiO}_2$  (B) and  $\text{TiO}_2$  (B)-graphene nanoscrolls are shown in Fig. 5. The charge and discharge voltage curves of the bare  $\text{TiO}_2$  (B) at different rates from  $0.1 \text{ C}$  to  $10 \text{ C}$  ( $1 \text{ C} = 335 \text{ mA g}^{-1}$ ) within a cut-off voltage window of  $1.0$ – $3.0$  V are displayed in Fig. 5(a), exhibiting discharge and charge capacity of  $257$  and  $228 \text{ mAh g}^{-1}$  at  $0.1 \text{ C}$ , respectively. The irreversible capacity loss can be attributed to the reactions between the surface of the  $\text{TiO}_2$  (B) and the electrolytes, but not  $\text{Li}$  trapped in the

nanostructures [30]. After  $300$  cycles at  $10 \text{ C}$  rate, the reversible capacity of the bare  $\text{TiO}_2$  (B) still remains  $85 \text{ mAh g}^{-1}$  (Fig. 5(b)).  $\text{TiO}_2$  (B)-graphene nanoscrolls present initial specific discharge and charge capacity of  $272$  and  $232 \text{ mAh g}^{-1}$  at  $0.1 \text{ C}$ , respectively (Fig. 5(c)). A capacity loss of about  $40 \text{ mAh g}^{-1}$  is found in the first cycle, which is mainly attributed to the side reactions between  $\text{TiO}_2$  (B) nanowires and the electrolytes, as  $\text{H}_2\text{O}$  and  $\text{O}-\text{H}$  groups remained on the surface of  $\text{TiO}_2$  (B) [30]. However, the initial coulombic efficiency at  $0.1 \text{ C}$  reaches  $85\%$ , which is much higher than previous report [20]. It can be postulated that graphene nanoscrolls effectively restrict the side reactions between hydroxyl groups on the surface of  $\text{TiO}_2$  (B) nanowires and the electrolytes, consequently decrease the irreversible capacity loss [30]. Two flat voltage plateaus at around  $1.7 \text{ V}$  and  $1.9 \text{ V}$  are observed in the charge/discharge plots, respectively, corresponding to the lithium insertion and extraction in the anatase phase [39]. The reversible capacity increases obviously in the sloped regions of  $1.75$ – $1.0 \text{ V}$  and  $1.0$ – $1.9 \text{ V}$  due to fast pseudocapacitive process of lithium storage (Fig. 5(d)). As shown in Fig. 5(e), the  $\text{TiO}_2$  (B)-graphene nanoscrolls deliver specific capacity of  $195$ ,  $176$ ,  $157$ ,  $145$  and  $135 \text{ mAh g}^{-1}$  at  $0.5$ – $10 \text{ C}$  rates respectively, much higher than that of the bare  $\text{TiO}_2$

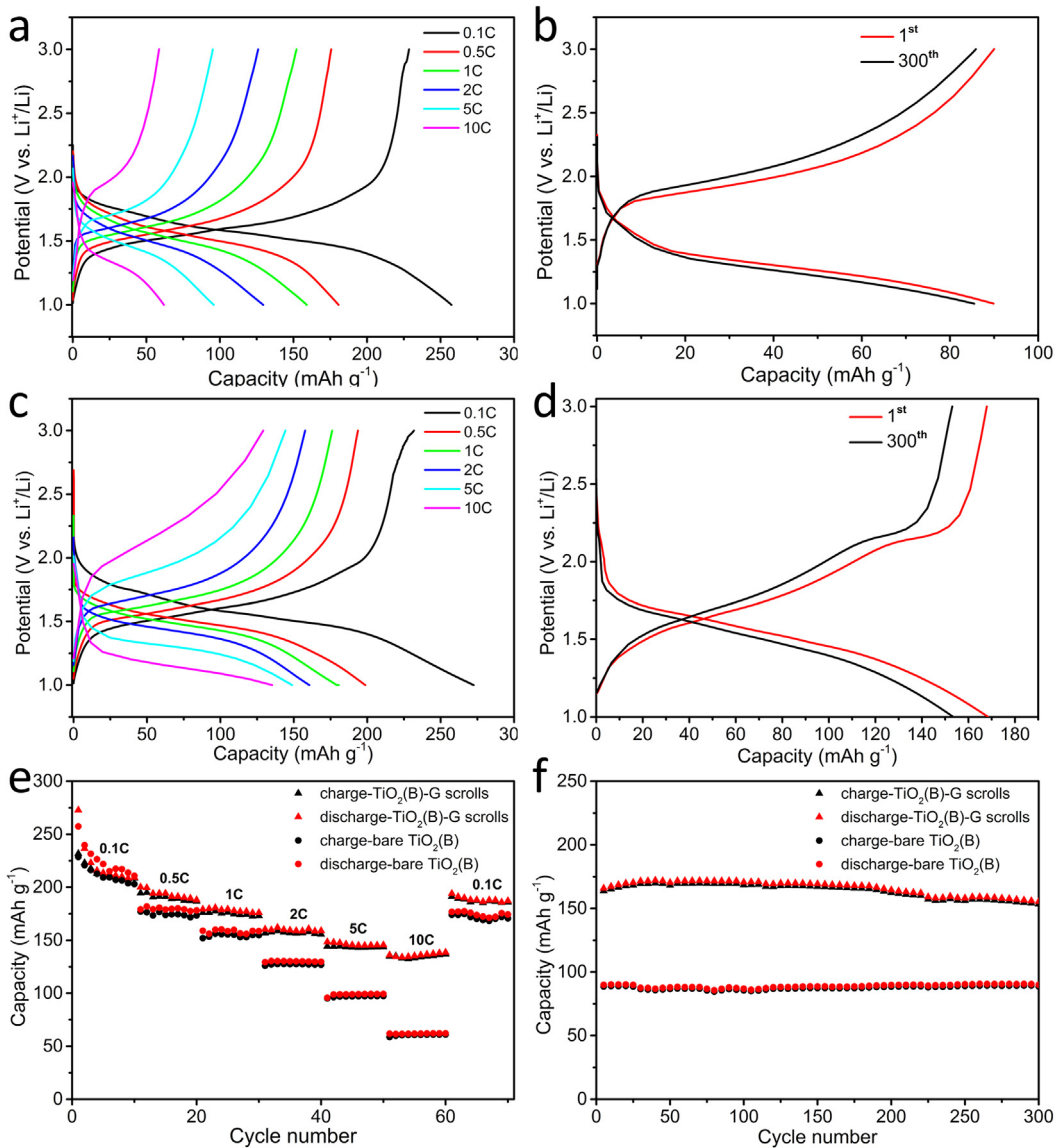


**Fig. 5.** Charge/discharge voltage curves of bare  $\text{TiO}_2$  (B) (a) from 0.1 C to 10 C, (b) in the 1st, 300th cycles at 10 C and  $\text{TiO}_2$  (B)-graphene nanoscrolls (c) from 0.1 C to 10 C, (d) in the 1st, 300th cycles at 10 C; (e) rates performances and (f) charge/discharge cycling performances of bare  $\text{TiO}_2$  (B) and  $\text{TiO}_2$  (B)-graphene nanoscrolls at 10 C between 1.0 and 3.0 V.

(B) (177, 152, 126, 95 and 60  $\text{mAh g}^{-1}$  at 0.5–10 C rates, respectively), suggesting that the encapsulation of graphene nanoscrolls in the composites play a vital role in the improvement of rate capability. The cycling performances of the bare  $\text{TiO}_2$  (B) and  $\text{TiO}_2$  (B)-graphene nanoscrolls electrode at 10 C rate are presented in Fig. 5(f). The cycling capacity of  $\text{TiO}_2$  (B)-graphene nanoscrolls at 10 C is about 153  $\text{mAh g}^{-1}$ , which is higher than the data from the test of rate capability (135  $\text{mAh g}^{-1}$ ). In the test of rate capability, the reversible  $\text{Li}^+$  capacity strongly depend on the  $\text{Li}^+$  diffusion rate in the bulk at different charge–discharge current. The discharge  $\text{Li}^+$  capacity tend to decrease with the increase of charge–discharge current. The loss of reversible  $\text{Li}^+$  at 1 C, 2 C and 5 C causes the difference in the electrochemical capacity at 10 C rate, which is accordance with previous literature [18,20]. The specific capacity of  $\text{TiO}_2$  (B)-graphene nanoscrolls is much higher than that of the bare  $\text{TiO}_2$  (B). To  $\text{TiO}_2$  (B)-graphene nanoscrolls, slight increase can be seen during the first several cycles, associating with the electrochemical activation of  $\text{TiO}_2$  (B) nanowires which are anchored closely with oxidized graphene. Kavan L. et al. also found that the

electrochemical performance of  $\text{TiO}_2$  was improved by carbon nanotubes networking when  $\text{TiO}_2$  are anchored on the surface of oxidized carbon nanotubes [27]. After 300 cycles at 10 C, it still remains a high reversible capacity of 153  $\text{mAh g}^{-1}$  with capacity retention of 94%. The excellent electrochemical performance can be attributed to the synergetic effect [44] between graphene nanoscrolls and  $\text{TiO}_2$  (B) nanowires. The porous graphene nanoscrolls on the outside provide abundant lithium ion insertion sites and enhance the electronic conductivity of the composites as well.  $\text{Li}^+$  insertion can occur not only in the end planes, but also through the porous graphene nanoscrolls. Meanwhile,  $\text{TiO}_2$  (B) nanowires show typical pseudocapacitive behavior, hence remarkably improving the electrochemical performance of the composites.

#### 4. Conclusions

In summary, we have successfully constructed coaxial  $\text{TiO}_2$  (B)-graphene nanoscrolls nanoarchitectures under hydrothermal treatment, followed by ion-exchange and heat treatment. The

thickness of tubular graphene nanoscrolls beyond  $\text{TiO}_2$  (B) nanowires is dependent on the initial graphene layers and the driving force from dangling bonds on the surface of titanates. The tightly encapsulated graphene nanoscrolls effectively restrict the electrical isolation between the substrate and active materials, thus stabilize the structure of the composites. The nanoscrollled architectures facilitate lithium ions transport, as well as alleviate the volume change during fast lithiation and delithiation, leading to the improvement of the electrochemical performance of the composites. This facile and template-free method will be promising to synthesize graphene nanoscrolls-based composites for energy storage and dye-sensitive solar cells.

## Acknowledgments

This work is financially supported by the National Natural Science Foundation of China (No. 51172293) and the Fundamental Research Funds for the Central Universities of China (No. CDJZR 12 225501 & No. CDJZR 13 130027). And the authors appreciate the technical support from the Laboratory of New Energy Materials, Chongqing University, China.

## Appendix A. Supplementary data

Supplementary data related to this article can be found at <http://dx.doi.org/10.1016/j.jpowsour.2014.06.056>.

## References

- [1] N.-S. Choi, Z. Chen, S.A. Freunberger, X. Ji, Y.-K. Sun, K. Amine, G. Yushin, L.F. Nazar, J. Cho, P.G. Bruce, *Angew. Chem. Int. Ed.* 51 (2012) 9994–10024.
- [2] S.-H. Lee, H.-G. You, K.-S. Han, J. Kim, I.-H. Jung, J.-H. Song, *J. Power Sources* 247 (2014) 307–313.
- [3] G.-N. Zhu, Y.-G. Wang, Y.-Y. Xia, *Energy Environ. Sci.* 5 (2012) 6652–6667.
- [4] H. Xia, M. Lai, L. Lu, *J. Mater. Chem.* 20 (2010) 6896–6902.
- [5] Z. Yang, D. Choi, S. Kerisit, K.M. Rosso, D. Wang, J. Zhang, G. Graff, J. Liu, *J. Power Sources* 192 (2009) 588–598.
- [6] L. Kavan, *Chem. Rec.* 12 (2012) 131–142.
- [7] S. Liu, Z. Wang, C. Yu, H.B. Wu, G. Wang, Q. Dong, J. Qiu, A. Eychmüller, X.W. Lou, *Adv. Mater.* 25 (2013) 3462–3467.
- [8] L. Kavan, *J. Solid State Electrochem.* (2014), <http://dx.doi.org/10.1007/s10008-014-2435-x>.
- [9] M. Zukalová, M. Kalbáč, L. Kavan, I. Exnar, M. Graetzel, *Chem. Mater.* 17 (2005) 1248–1255.
- [10] B. Laskova, M. Zukalova, A. Zukal, M. Bousa, L. Kavan, *J. Power Sources* 246 (2014) 103–109.
- [11] J. Wang, J. Polleux, J. Lim, B. Dunn, *J. Phys. Chem. C* 111 (2007) 14925–14931.
- [12] Y. Qiu, K. Yan, S. Yang, L. Jin, H. Deng, W. Li, *ACS Nano* 4 (2010) 6515–6526.
- [13] Y. Ren, L.J. Hardwick, P.G. Bruce, *Angew. Chem.* 122 (2010) 2624–2628.
- [14] L. He, R. Ma, N. Du, J. Ren, T. Wong, Y. Li, S.T. Lee, *J. Mater. Chem.* 22 (2012) 19061–19066.
- [15] Y. Ren, Z. Liu, F. Pourpoint, A.R. Armstrong, C.P. Grey, P.G. Bruce, *Angew. Chem. Int. Ed.* 51 (2012) 2164–2167.
- [16] A.G. Dylla, P. Xiao, G. Henkelman, K.J. Stevenson, *J. Phys. Chem. Lett.* 3 (2012) 2015–2019.
- [17] A.R. Armstrong, G. Armstrong, J. Canales, R. García, P.G. Bruce, *Adv. Mater.* 17 (2005) 862–865.
- [18] K. Shin, H.J. Kim, J.-M. Choi, Y.-M. Choi, M.S. Song, J.H. Park, *Chem. Commun.* 49 (2013) 2326–2328.
- [19] G. Armstrong, A.R. Armstrong, J. Canales, P.G. Bruce, *Chem. Commun.* 0 (2005) 2454–2456.
- [20] S. Liu, H. Jia, L. Han, J. Wang, P. Gao, D. Xu, J. Yang, S. Che, *Adv. Mater.* 24 (2012) 3201–3204.
- [21] A.G. Dylla, J.A. Lee, K.J. Stevenson, *Langmuir* 28 (2012) 2897–2903.
- [22] S. Ding, J.S. Chen, D. Luan, F.Y.C. Boey, S. Madhavi, X.W. Lou, *Chem. Commun.* 47 (2011) 5780–5782.
- [23] X. Xin, X. Zhou, J. Wu, X. Yao, Z. Liu, *ACS Nano* 6 (2012) 11035–11043.
- [24] H. Huang, J. Fang, Y. Xia, X. Tao, Y. Gan, J. Du, W. Zhu, W. Zhang, *J. Mater. Chem. A* 1 (2013) 2495–2500.
- [25] J. Wang, Y. Zhou, B. Xiong, Y. Zhao, X. Huang, Z. Shao, *Electrochim. Acta* 88 (2013) 847–857.
- [26] H.-C. Tao, L.-Z. Fan, X. Yan, X. Qu, *Electrochim. Acta* 69 (2012) 328–333.
- [27] L. Kavan, R. Bacsá, M. Tunckol, P. Serp, S.M. Zakeeruddin, F. Le Formal, M. Zukalova, M. Graetzel, *J. Power Sources* 195 (2010) 5360–5369.
- [28] J.S. Chen, Z. Wang, X.C. Dong, P. Chen, X.W. Lou, *Nanoscale* 3 (2011) 2158–2161.
- [29] S. Yang, X. Feng, K. Müllen, *Adv. Mater.* 23 (2011) 3575–3579.
- [30] S. Brutti, V. Gentili, H. Menard, B. Scrosati, P.G. Bruce, *Adv. Energy Mater.* 2 (2012) 322–327.
- [31] Z. Kang, E. Wang, L. Gao, S. Lian, M. Jiang, C. Hu, L. Xu, *J. Am. Chem. Soc.* 125 (2003) 13652–13653.
- [32] H. Shioyama, T. Akiti, *Carbon* 41 (2003) 179–181.
- [33] L.M. Viculis, J.J. Mack, R.B. Kaner, *Science* 299 (2003) 1361.
- [34] F. Zeng, Y. Kuang, Y. Wang, Z. Huang, C. Fu, H. Zhou, *Adv. Mater.* 23 (2011) 4929–4932.
- [35] F. Zeng, Y. Kuang, G. Liu, R. Liu, Z. Huang, C. Fu, H. Zhou, *Nanoscale* 4 (2012) 3997–4001.
- [36] A. Bagri, C. Mattevi, M. Acik, Y.J. Chabal, M. Chhowalla, V.B. Shenoy, *Nat. Chem.* 2 (2010) 581–587.
- [37] Y. Zhu, S. Murali, M.D. Stoller, K.J. Ganesh, W. Cai, P.J. Ferreira, A. Pirkle, R.M. Wallace, K.A. Cychoz, M. Thommes, D. Su, E.A. Stach, R.S. Ruoff, *Science* 332 (2011) 1537–1541.
- [38] X. Fan, W. Peng, Y. Li, X. Li, S. Wang, G. Zhang, F. Zhang, *Adv. Mater.* 20 (2008) 4490–4493.
- [39] H. Liu, Z. Bi, X.-G. Sun, R.R. Unocic, M.P. Paranthaman, S. Dai, G.M. Brown, *Adv. Mater.* 23 (2011) 3450–3454.
- [40] D. Wang, D. Choi, J. Li, Z. Yang, Z. Nie, R. Kou, D. Hu, C. Wang, L.V. Saraf, J. Zhang, I.A. Aksay, J. Liu, *ACS Nano* 3 (2009) 907–914.
- [41] A.G. Dylla, G. Henkelman, K.J. Stevenson, *Acc. Chem. Res.* 46 (2013) 1104–1112.
- [42] J. Li, W. Wan, H. Zhou, J. Li, D. Xu, *Chem. Commun.* 47 (2011) 3439–3441.
- [43] C. Arrouvel, S.C. Parker, M.S. Islam, *Chem. Mater.* 21 (2009) 4778–4783.
- [44] S. Yang, W. Yue, J. Zhu, Y. Ren, X. Yang, *Adv. Funct. Mater.* 23 (2013) 3570–3576.